Article

Rainstorm Resistance of Recycled Pervious Concrete under the Coupling of Fatigue and Freeze–Thaw Cycles

Kai-Lin Huang, Yang Song * and Yan-Min Sheng

School of Civil and Architectural Engineering, Changzhou Institute of Technology, Changzhou 213032, China;
huangkl@czu.cn (K.-L.H.); shengym@czu.cn (Y.-M.S.)
* Correspondence: songy@czu.cn

Abstract: In order to alleviate the increasing serious urban waterlogging problem, the rainstorm resistance of a new self-compacting recycled pervious concrete (NSRPC) under the coupling of freeze–thaw (F-T) and fatigue is studied. The once-in-a-century rainfall was simulated, and the rainstorm resistance of NSRPC was evaluated mainly through the ponding depth and drainage time. In addition, the mechanical properties (compressive strength and flexural strength), mass loss rate and relative dynamic elastic modulus of NSRPC during F-T and fatigue coupling were measured. The microstructure of NSRPC was observed by scanning electron microscopy, and its deterioration mechanism was analyzed. The results show that the fatigue load aggravates the F-T damage of NSRPC in the later stage. With the increase in the number of fatigue cycles, the loss rate of compressive strength and flexural strength of NSRPC increases continuously, and the permeability coefficient decreases first and then increases. With the increase in the number of freeze–thaw and fatigue cycles, the mass loss rate increases gradually, and the relative dynamic elastic modulus decreases gradually. After the coupling of fatigue and F-T cycles, the minimum mass loss of NSRPC is only 2.14%, and the relative dynamic elastic modulus can reach 86.2%. The increase in the number of fatigue cycles promotes the generation and expansion of micro-cracks and provides more channels for water to invade the matrix. Under the action of rainstorm in the 100-year return period, the maximum ponding depth of NSRPC with steel fiber content is 84 mm, and the drainage time is 7.1 min, which meets the needs of secondary highway. This study will provide theoretical basis for improving the service life and drainage capacity of urban drainage pavement in cold areas.

Keywords: recycled pervious concrete; rainstorm resistance; fatigue; freeze–thaw cycle

1. Introduction

In the field of urban transport infrastructure, traditional impervious pavements cover most of the natural surface [1–4]. Due to the low permeability and air permeability of traditional pavement, most of the rainwater is difficult to reach the natural surface, preventing the exchange in heat and moisture between soil and air [5]. Cities have poor regulation of temperature and humidity, and the urban heat island effect is becoming more prominent. During rainfall, the water cannot permeate the soil and reach the surface, leading to a decrease in groundwater levels and a continuous increase in surface runoff [6]. In China, currently, two-thirds of the region is facing the risk of urban flooding [7], and over 62% of cities have experienced heavy rainfall-induced flooding disasters [8]. It is estimated that by 2050, the economic losses caused by heavy rainfall-induced flooding will increase to 158 billion dollars [9], which is a grave situation.

Owing to the porous structure and superior permeability of pervious concrete, numerous nations are advocating for its substitution of impervious setting concrete and tarmac roads, aiming to mitigate the damages brought about by flash floods [10]. Contrasted with impervious roads, the use of pervious concrete surfaces can diminish run-off by up to 93% [11]. Amid heavy rainfall, pervious concrete pavements cannot solely minimize

run-off but abolish most of the storm run-off genesis [12]. Meanwhile, pervious concrete has achieved success in light load traffic areas such as parking lots and footpaths [13,14]. In contrast with conventional concrete, the strength and durability of pervious concrete are generally inferior, hence limiting its scope of application [15]. A novel high-strength pervious concrete was proposed, which through the introduction of vertical artificial pore channels within a high-strength concrete matrix not only maintains considerable resilience, but the continuous vertical channels simultaneously yield outstanding permeability as well [16]. Based on the aforementioned research, a novel self-compacting recycled pervious concrete (NSRPC) is produced in this study, by introducing self-compacting concrete as a substrate, and employing 100% recycled coarse aggregate as a replacement for natural aggregate. NSRPC ensures permeability through the introduction of man-made channels, thereby negating the need to reduce fine aggregates to enhance porosity. Moreover, it exudes a high degree of permeability (>2 cm/s) and strength (>50 MPa), with its permeability coefficient being tenfold that of traditional pervious concrete, and its strength being twice as strong in the same porosity [17]. Concurrently, it possesses exceptional durability; given the durability coefficient, NSRPC can be employed in cold climates for up to 100 years [18]. Compared to traditional pervious concrete, NSRPC demonstrates improved clog resistance, with most clogging materials successfully traversing the channels instead of remaining within the NSRPC paths. Due to these exemplary characteristics, NSRPC holds the potential for utilization in sophisticated environments subjected to fatigue or freeze–thaw (F-T) cycles, such as airport runways, highways, and bridge decks. Importantly, this facilitates the use of pervious concrete in heavy-duty roads.

In China, almost half of regions fall within cold zones [19] with the deterioration caused by F-T cycles being one of the major reasons for the limited application of pervious concrete [20,21]. The substantial porosity of pervious concrete contributes to the degree of damage it sustains in F-T conditions being significantly more severe than typical concrete [22]. Upon freezing, the free water within the cement paste between the coarse aggregates in the pervious concrete expands, leading to the generation of micro-cracks. With increasing frequency of F-T cycles, the incidence of these cracks multiplies, culminating in structural damage [13,23]. As time advances, fines accumulate on the surface, progressively blocking the pores of the pervious pavement with low F-T durability [24], substantially mitigating the pavement's permeability [25]. Furthermore, due to the substantial specific surface area, there is an abundance of capillary pores within pervious concrete. The expansion force generated by water freezing in low-temperature environments leads to an accumulated damage within the pervious concrete causing aggregates or mortars to peel off and reside in the highly curved channels, thus hindering its permeability and reducing rainfall flood resistance. Feo et al. [20] examined the frost resistance and flexural performance of concrete with distinct steel fiber (SF) capacities (0%, 1.25 vol.%, and 2.5 vol.%) and found that steel fiber-reinforced concrete has superior crack resistance and energy absorption capability compared to ordinary concrete. Hesami et al. [26] modified pervious concrete using 0.5% SF and found that the flexural strength of the fortified pervious concrete was approximately 22% higher than that of the unmodified mix, while the permeability remained almost constant. Thus, SF is effective in improving the frost resistance of pervious concrete. However, there is a notable scarcity of reports on the frost resistance of pervious concrete with continuous pores; this then necessitates the exploration of the appropriateness of SF in such concrete.

Pervious concrete pavement is predominantly employed in areas subject to lighter traffic loads, such as pedestrian walkways, parking lots, and park precincts, while it is sparingly utilized for higher-grade roadways. This is invariably due to the suboptimal initial performance characteristics of pervious concrete [27,28]. A surfeit of engineering practice has unveiled that pervious concrete pavements are susceptible to fatigue or recurrent load-induced degradation, often prematurely manifesting maladies, such as thermal shrinkage cracks and damp shrinkage cracks [29]. On a plethora of heavy traffic arteries, large-scale exfoliation of the pervious pavement's surface occurs often within less than five

years. Numerous roadways commence manifesting damages, disfigurations, and deterioration shortly after service inception. This deleteriously impacts the lifespan of pavement and substantially diminishes its longevity and permeability. Research findings indicate that early-stage maladies of pervious concrete pavements are predominantly correlated with fatigue or recurrent loading, which has emerged as the most significant and prevalent type of damage [30]. One principal cause of the aforementioned degradation is that the pervious pavement surface possesses poor fatigue resistance and lacks robustness to adequately resist the vehicular load-induced shear stress on the pervious concrete pavement surface, leading to problems like aggregate exfoliation or loosening, subsequently resulting in surface damage [31]. Consequently, studying the fatigue resistance of pervious concrete pavements holds considerable importance and is anticipated to contribute positively to mitigate the occurrence of early-stage maladies in pervious concrete pavements.

This study carries out an analysis of the impact on mechanical characteristics, permeability, and F-T durability of NSRPC containing five different proportions of SF, simulating a deluge with a return period of 100 years and a duration of 60 min. The evaluation of the rainstorm resistance of NSRPC under the coupling of (F-T) and fatigue is based on the ponding depth and drainage time. In addition, the frost resistance of NSRPC was evaluated by mass loss rate and relative dynamic elastic modulus. Finally, the microstructure of NSRPC after the coupling of F-T and fatigue was observed by scanning electron microscopy, and its deterioration mechanism was analyzed.

2. Experimental Program

2.1. Materials

Recycled coarse aggregate (RCA), purchased from a solid waste treatment firm in Changzhou, China, was meticulously cleansed, dried, and sifted in a laboratory environment to secure fraction with a granular size of 5–16 mm. The macroscopic appearance and grading curve of the RCA are vividly portrayed in Figure 1a,b, respectively. The physical properties of the RCA were tested in strict accordance with Chinese standard GB/T 25177-2010 [32], the results of which are tabulated in Table 1. River sand featuring a fineness modulus of 2.3 was utilized as fine aggregate. Ordinary Portland cement (OPC) with a strength grade of P.O 52.5, fly ash, and silica fume were employed as binding materials. Figure 2 presents the particle distribution of each binding material. The chemical composition of the binding materials can be referred to in Table 2. Furthermore, SF with a diameter of 0.2 mm, length of 5 mm, and tensile strength of 2850 MPa were imbued to enhance the mechanical properties of the concrete. Moreover, superplasticizer (SP) was adopted to improve the workability of the concrete.
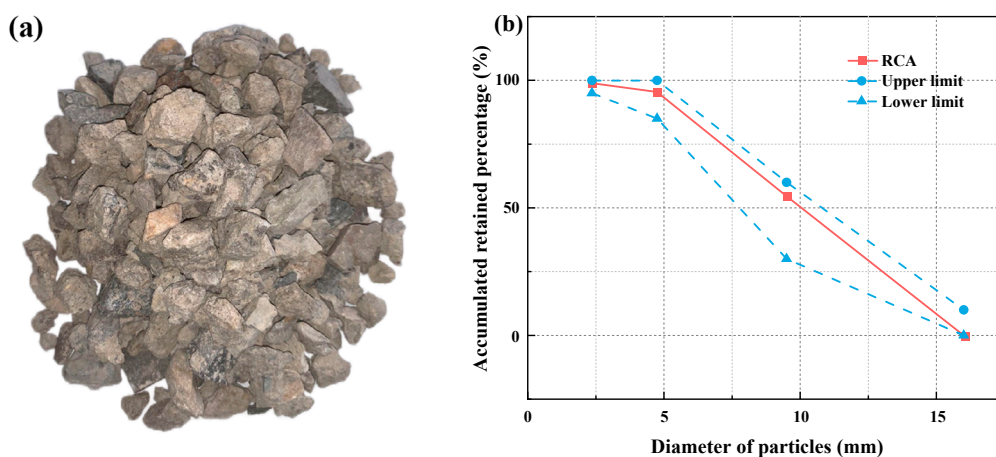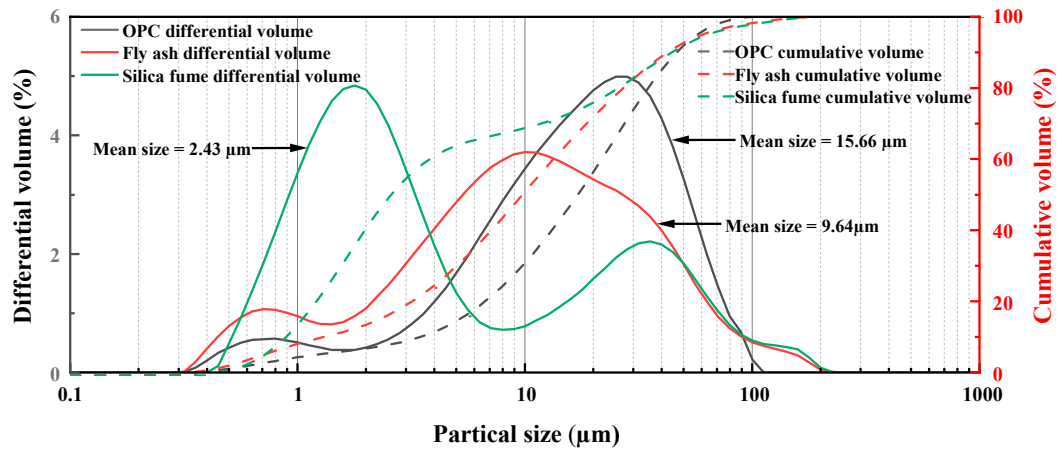

Figure 1. Macrostructure and grading curve of RCA: (**a**) macrostructure, (**b**) grading curve.

Table 1. Physical properties of RCA.

Properties	Apparent Density (kg/m³)	Bulk Density (kg/m³)	Water Absorption (%)	Crushing Index (%)
RCA	2567	1237	6.6	14.5

Figure 2. Particle size distributions of OPC, fly ash, and silica fume.

Table 2. Chemical compositions of OPC, fly ash, and silica fume (%).

Item	CaO	SiO$_2$	Al$_2$O$_3$	Fe$_2$O$_3$	SO$_3$	MgO	TiO$_2$	K$_2$O
OPC	53.73	21.46	9.65	5.73	3.22	3.07	0.64	0.67
Fly ash	3.74	52.61	28.13	3.55	1.79	1.22	0.96	1.73
Silica fume	0.07	95.78	0.23	0.12	0.02	-	0.02	-

2.2. Mix Proportion and Specimen Preparation

In this experiment, the target strength for NSRPC is set at 60 MPa with a filling ability achieving SF2. Five different SF dosages were selected, namely 0, 0.5 vol.%, 1 vol.%, 1.5 vol.%, and 2 vol.%, with the specific mix proportions provided in Table 3. The fabrication of specimens employed the method of pre-embedded rebar with designed holes. That is, rebar was firstly inserted into pre-determined concrete molds, which was followed by pouring the mixed material into the mold, and the rebar was pulled out before the final setting. It is noteworthy that the pre-embedded rebar length should be greater than 1.5 times the concrete width; otherwise, the rebar is likely to fall off in the hole during pouring. The porosity of NSRPC is set at 1.13% with a rebar diameter of 3 mm, and the specimens of two sizes prepared were 100 mm × 100 mm × 400 mm and 100 mm × 100 mm × 100 mm, with hole distributions of 4 × 16 and 4 × 4 respectively. The model and physical diagram of the specimen is depicted in Figure 3. After shaping, the specimens were placed into a standard curing room for 24 days. Upon completion of curing, they were soaked in clean water for 4 days to reach a state of saturation before removal.

Table 3. Mix proportion of NSRPC (kg/m³).

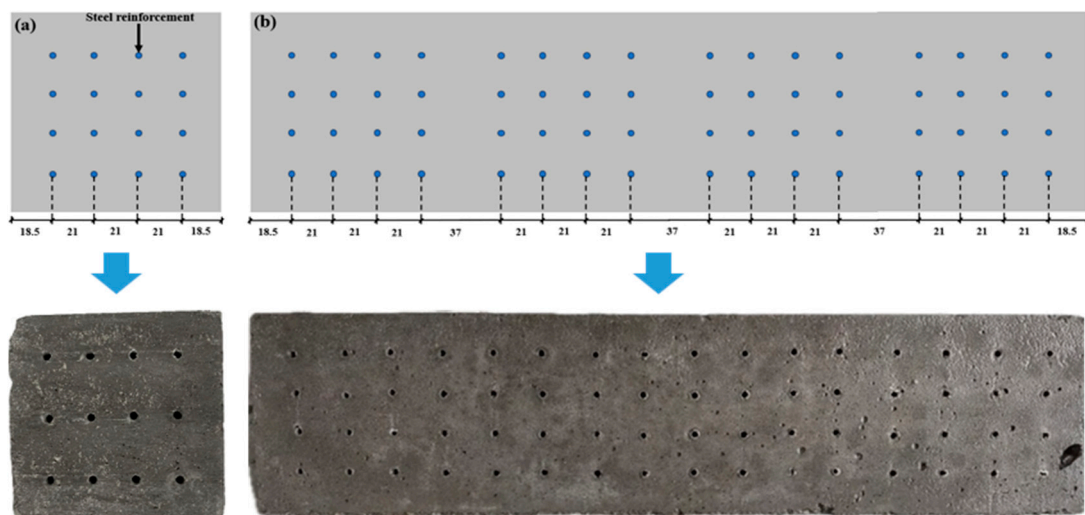| Mixtures	RCA	Sand	Water	Cement	Fly Ash	Silica Fume	SF	SP	Slump (mm)
0-PC	770	840	189	387	89	60	0	4.7	146
0.5-SF-PC	770	840	189	387	89	60	39	4.7	134
1-SF-PC	770	840	189	387	89	60	78	4.7	127
1.5-SF-PC	770	840	189	387	89	60	117	4.7	120
2-SF-PC	770	840	189	387	89	60	156	4.7	108

Figure 3. Model and physical diagram of the specimen: (**a**) cube specimen, (**b**) prism specimen.

2.3. Test Methods

2.3.1. Mechanical Properties Test

Employing the electro-hydraulic servo universal testing machine and in alignment with GB/T 50081-2019 [33], the initial compressive and flexural strengths of the NSRPC is examined as well as following 300 F-T cycles. The dimensions of the specimens under examination are 100 mm × 100 mm × 100 mm, with loading pace, respectively, being 0.8 MPa/s and 0.08 MPa/s. It is crucial to denote that the samples used to test the compressive and flexural strengths of the NSRPC post F-T and fatigue cycles are derived from specimens sized at 100 mm × 100 mm × 400 mm; their cutting surface is delineated in Figure 4. The specific cutting method is to cut the specimen into 4 parts along the cutting surface with a cutting machine.
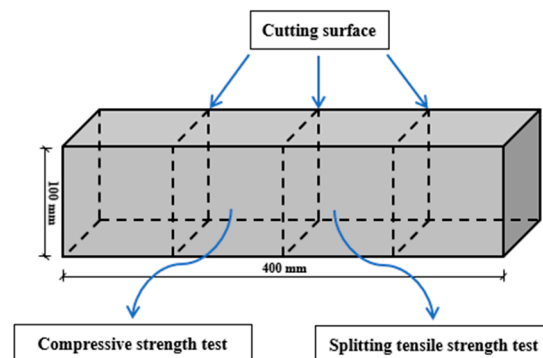

Figure 4. Selection of test specimens for mechanical properties after F-T and fatigue cycles.

2.3.2. Freeze–Thaw Cycle and Fatigue Coupling Test

The F-T cycle experiment was conducted in accordance with GB/T 50082-2009 [34], where the temperature range for freezing and thawing extended from (−18 ± 2 °C) to (5 ± 2 °C). The mass of the specimens, as well as the dynamic modulus of elasticity, was measured after every 50 cycles of freezing and thawing. Subsequent calculations pertaining to the mass loss percentage and relative dynamic modulus of elasticity were carried out by Equations (1) and (2), respectively. It is imperative to note that encountering each instance of removing the specimen from the F-T chamber for testing, the specimen's position should be inversed prior to proceeding with subsequent F-T examinations.

$$\text{relative dynamic elastic modulus (n)} = \frac{f_n^2}{f_0^2} \times 100\% \tag{1}$$

$$\text{mass loss rate (n)} = \frac{m_0 - m_n}{m_0} \times 100\% \tag{2}$$

where relative dynamic elastic modulus (n) is the relative dynamic elastic modulus after n F-T cycles (%), mass loss rate (n) is the mass loss rate after n F-T cycles (%), f_n is the transverse fundamental frequency after n F-T cycles (Hz), m_n is the mass after n F-T cycles (kg), f_0 is the initial transverse fundamental frequency (Hz), and m_0 is the initial mass (kg).

At present, China's transportation is characterized by axle loading and overloading. When the stress level surpasses 0.5, the internal fissures within the concrete pavement persistently broaden, eventually leading to the fracture of the concrete roadway. Concrete pavements in certain areas under heavy loading experience stress levels as high as 0.6 under vehicular loads, leading to substantial cup-shaped destruction of the concrete pavement. Accordingly, the NSRPC was subjected to 2×10^5 iterations of flexural fatigue testing under a sinusoidal wave shape, at a frequency of 10 Hz, with a stress level of 0.6 (S = f_{max}/f_f), and a minimum stress ratio of 0.2 ($S_{min} = f_{min}/f_f$). The fatigue testing for the NSRPC is illustrated in Figure 5.
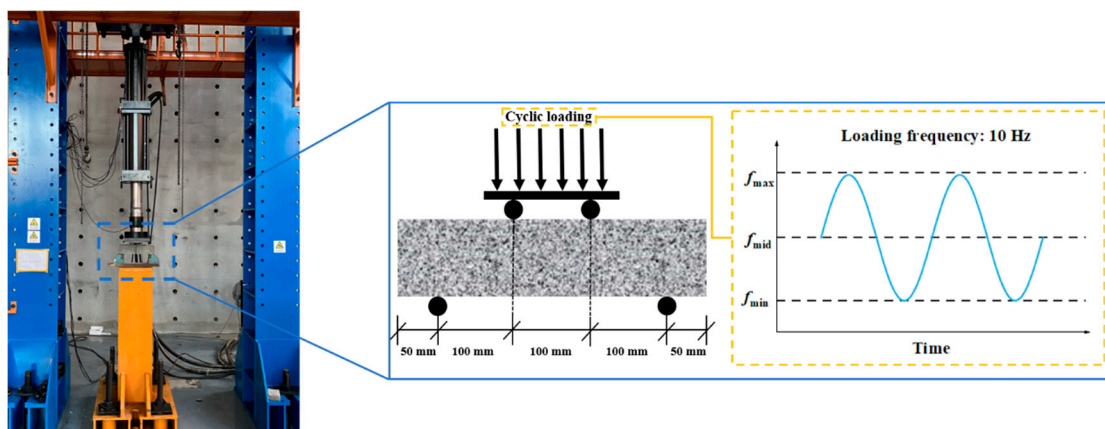

Figure 5. Process of fatigue test.

2.3.3. Heavy Rainfall Experiment

The current experiment selected a heavy rainfall with a return period of 100 years for flood resistance design. The duration of the storm is a span of 60 min, which is suitable for the majority of urban drainage systems [35]. Figure 6a showcases the apparatus employed for the artificial simulation of rainfall. Prior to the experiment, preservation film is wrapped around the impervious surface surrounding the specimens. Subsequently, the wrapped test blocks are positioned upon the support frame of the catchment tank, which is crafted from cylindrical acrylic sheet. The intensity of the rainfall alters every five minutes with the specifics of the rainfall intensity depicted in Figure 6b.

2.4. Microstructure Test

The microscopic structures of NSRPC post the coupling of F-T and fatigue cycles were inspected utilizing a scanning electron microscope (Regulus-8100). Samples, each measuring approximately 5 mm × 5 mm × 3 mm, were meticulously selected from NSRPC, which was followed by a 24 h drying process within an oven set at 60°C. Prior to examination, each sample underwent a gold-spraying treatment. The course of the experiment entailed observing the transition zones and micro-cracks present within each specimen.
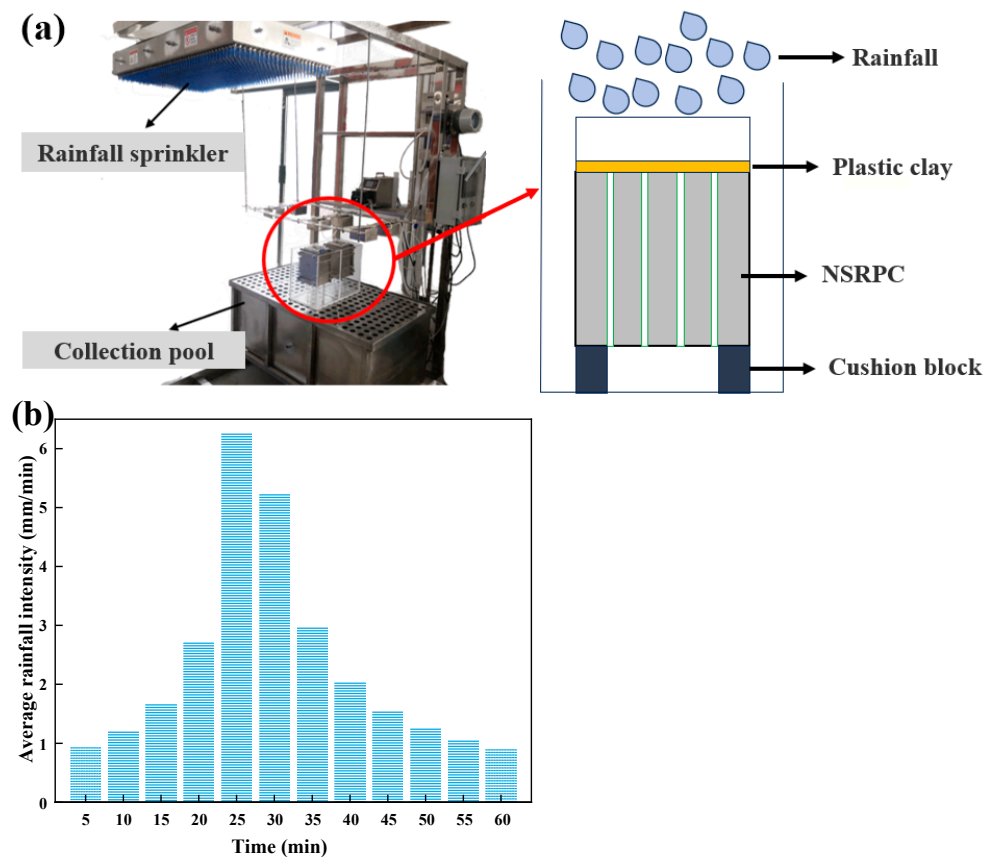
Figure 6. Heavy rainfall experiment: (**a**) artificial rain device, (**b**) average rainfall intensity.

3. Results and Discussion

3.1. Mechanical Properties

3.1.1. Compressive Strength

The compressive strength of NSRPC under the coupling of F-T and fatigue cycles is illustrated in Figure 7. Figure 7a reveals that with the increase in fatigue cycles, the compressive strength of the NSRPC before F-T cycles first experiences a surge before plummeting. When the number of fatigue cycles reached 5×10^4, the compressive strength of 0-PC, 0.5-SF-PC, 1-SF-PC, 1.5-SF-PC, and 2-SF-PC ascended by 2.9%, 2.6%, 1.2%, 0.6%, and 1.1%, respectively, compared to their initial strengths. This could be ascribed to the fact that at a lower number of fatigue cycles, the fatigue load facilitated the preliminary healing of cracks within the concrete matrix, reducing the generation of cracks. In the ensuing F-T processes, the channels for water transportation consistently dwindled, thereby slightly enhancing frost resistance of NSRPC [36,37]. Nevertheless, with the escalation of the number of fatigue cycles, the exerted fatigue load engendered numerous novel micro-cracks within the NSRPC [38], providing a greater number of transportation routes for the penetration of water during F-T cycles. This led to previously isolated pores becoming interconnected [39].

After 300 F-T cycles, the compressive strength of NSRPC exhibited varying degrees of attenuation. Before fatigue cycles, the compressive strength of 0-PC, 0.5-SF-PC, 1-SF-PC, 1.5-SF-PC, and 2-SF-PC diminished by 34.3%, 28.4%, 22.7%, 17.1%, and 19.9%, respectively. As fatigue cycles increase, the detrimental impact of F-T cycle on the compressive strength of NSRPC intensified. At fatigue iterations of 2×10^5, the compressive strength of 0-PC, 0.5-SF-PC, 1-SF-PC, 1.5-SF-PC, and 2-SF-PC deteriorated by 41.5%, 30.9%, 28.7%, 20.5%, and 22.2%, respectively, compared with their pristine states prior to the F-T cycle. This implies that fatigue cycling exacerbated the F-T damage on NSRPC. Concurrently, continuous interior deterioration of the NSRPC matrix due to fatigue cycling lead to a decrease in inherent

cement matrix strength along with declining effective adhesive strength between the matrix and the aggregate, establishing permeation pathways for moisture, hence engendering suboptimal frost resistance of NSRPC [40]. With respect to all NSRPCs, the compressive strength continues to escalate with an increase in the concentration of SF, despite the damaging effects of combined fatigue and F-T cycling. The SF may counteract some tensile stress during fatigue, thereby decreasing the genesis of fatigue cracks and consecutively enhancing the compressive strength of NSRPC [41,42]. The subsequent loss rate in NSRPC compressive strength as a result of combined fatigue and F-T cycles is depicted in Figure 8. It reveals that the loss rate of 0-PC compressive strength reaches 24% after F-T cycling, while the loss rate of untarnished 0-PC is a mere 14%. Similar trends were observed with other mixtures, strongly insinuating that F-T cycling exacerbates the loss of NSRPC's compressive strength. To summarize, compared with unexposed NSRPC, following 2×10^5 fatigue and 300 F-T cycles, the compressive strength of 0-PC drops by 49.9%, while 1.5-SF-PC only experiences a 26.4% decline.
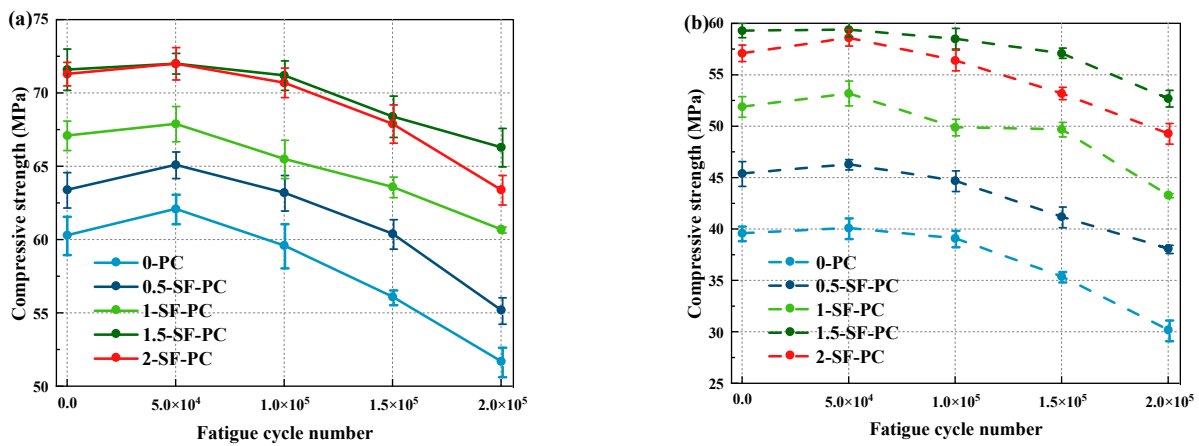

Figure 7. Compressive strength after coupling of fatigue and F-T cycles: (**a**) before F-T cycles; (**b**) after 300 F-T cycles.
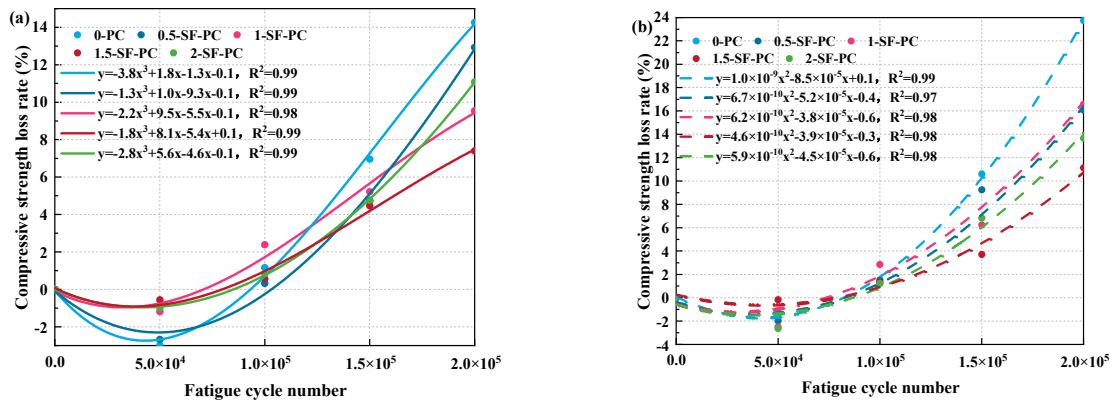

Figure 8. Compressive strength loss rate of NSRPC with the number of fatigue cycles before and after F-T: (**a**) before F-T cycles; (**b**) after 300 F-T cycles.

3.1.2. Flexural Strength

Contrary to its compressive strength, the NSRPC primarily resists bending moments via cross-sections oriented parallel to the pores, as delineated in Figure 9. The flexural strength of NSRPC following different F-T cycles and fatigue is represented in Figure 10. The flexural strength of NSRPC, without undergoing fatigue and F-T cycles, exceeds 6 MPa, thereby sufficiently meeting the bending requirements of heavy-load traffic roads ($\geq$5 MPa). Relative to the NSRPC unexposed to fatigue and F-T effects, following two hundred thousand fatigue cycles and 300 F-T cycles, the flexural strength of 0-PC fell by

51.5%, whilst that of 1.5-SF-PC declined merely by 29.7%. Such a phenomenon substantiates the fact that the incorporation of SF amplifies the fatigue and F-T durability of NSRPC.
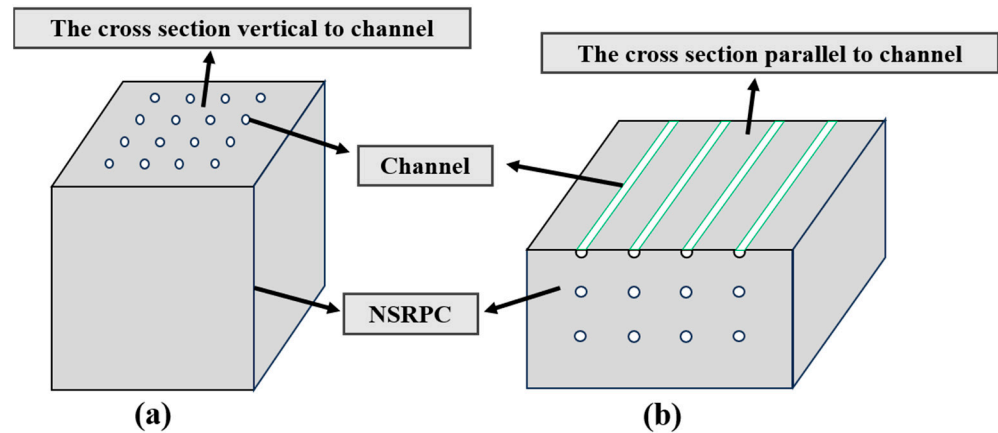

Figure 9. The cross-section of NSRPC: (**a**) vertical to channel; (**b**) parallel to channel.
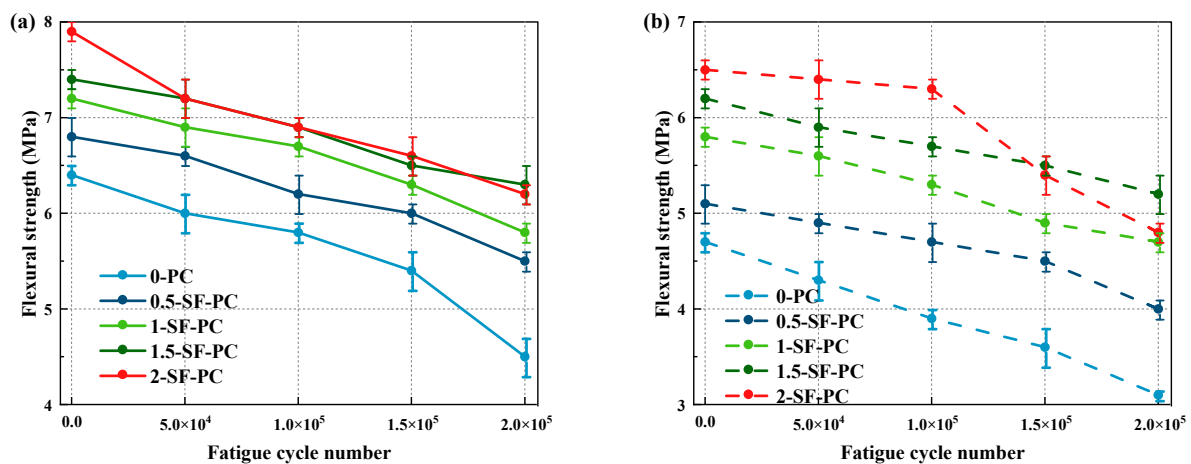

Figure 10. Flexural strength of NSRPC after coupling of fatigue and F-T cycles: (**a**) before F-T cycles; (**b**) after 300 F-T cycles.

When fatigue cycles were at 0, the flexural strength of 0-PC, 0.5-SF-PC, 1-SF-PC, 1.5-SF-PC, and 2-SF-PC fell, respectively, by 26.6%, 20.3%, 19.4%, 16.2%, and 17.7% post-F-T cycles. When fatigue cycles escalated to 2×10^5, the flexural strengths of the aforementioned specimens reduced, respectively, by 31.1%, 23.6%, 20.6%, 17.4%, and 22.5%. Figure 11 illustrates the loss rate of flexural strength of NSRPC before and after F-T cycles against fatigue cycles, thereby revealing that excluding 0-PC, the flexural strength loss rate before F-T cycles is significantly lower than that after F-T cycles. Such a conclusion emphasizes the crucial role of fatigue loading prior to F-T cycles in flexural strength; minor variations in 0-PC may likely instigate the amplified sensitivity of NSRPC toward flexural strength. When fatigue cycles are relatively smaller before the F-T stage, the discrepancy in the sectional resistance provided by effective sections is not conspicuous, causing minimal decline in flexural strength and rendering the variation in NSRPC flexural strength insignificant. For 0-PC, the flexural strength of NSRPC is at its nadir. This can be elucidated by recognizing that fatigue and F-T damage result in a noteworthy reduction in the effective cross-sectional area of NSRPC. Such a situation is tantamount to directly diminishing the tensile area of the lower part of NSRPC, resulting in a considerable fall in bending strength. A meager effective cross-sectional area is not conducive to the bending strength of NSRPC. Therefore, to acquire higher strength, it is recommended to moderately increase the SF dosage in pervious concrete, implying that cracks must evolve incessantly through steel fiber-reinforced mortar matrix.
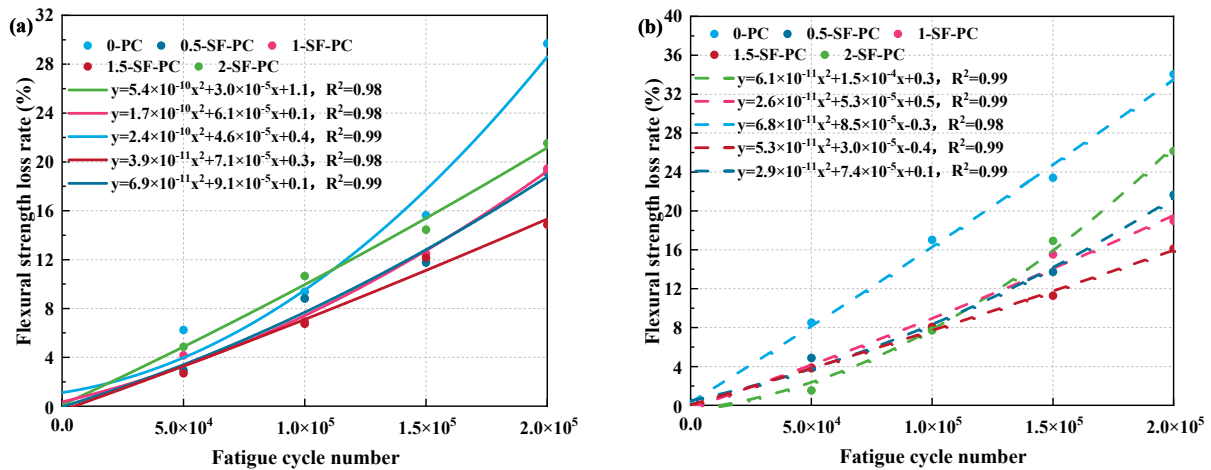
Figure 11. Flexural strength loss rate of NSRPC with the number of fatigue cycles before and after F-T: (**a**) before F-T cycles; (**b**) after 300 F-T cycles.

3.2. Mass Loss Rate

The mass loss rate of NSRPC represents the macroscopic damage effect, and it serves as one of the pivotal criterion for estimating intrinsic structural damage resultant from F-T cycles. The mass loss rate of NSRPC, post fatigue and F-T cycles, is delineated in Figure 12. In accordance with anticipations, amongst all mixtures, 0-PC, post 2×10^5 fatigue combined with 300 F-T cycles exhibited the highest mass loss rate, at 3.67%, whereas 2-SF-PC was the lowest, at a mere 2.14%. This intimates that the integration of SF can efficiently attenuate the mass depletion of NSRPC subsequent to the F-T. In instances where the number of fatigue cycles was 0, in contrast to the original mass loss rate not exposed to F-T cycles, a significant increase was observed in mass loss rate for 0-PC, 0.5-SF-PC, 1-SF-PC, 1.5-SF-PC, and 2-SF-PC, respectively. Moreover, with an enhancement in SF concentration, there was a gradual decrease in the mass loss rate of NSRPC, suggesting the effective mitigation of F-T-induced NSRPC mass loss by SF integration. When the F-T cycle was constant, an upward–downward fluctuation trend was apparent in the mass loss rate of NSRPC as the fatigue cycles increased. However, when the number of fatigue cycles went beyond 2×10^5, there was a notable upsurge in the mass loss rate of NSRPC.

In comparison to 0-PC, when experiencing 0 fatigue cycles and 300 F-T cycles, mass loss quotients of 0.5-SF-PC, 1-SF-PC, 1.5-SF-PC, and 2-SF-PC were reduced, respectively. This asserts that apprehending fatigue, along with the disruptive F-T effects, yields improved NSRPC durability, mitigates surface mortar particle exfoliation, subsequently curtailing moisture intrusion, and enhancing its ability to endure F-T cycles. As NSRPC possesses an expansive surface area owing to artificial pore paths as compared to ordinary concrete, fortifying these vulnerable regions and reducing their mass loss is paramount for the long-term durability.

3.3. Relative Dynamic Elastic Modulus

The relative dynamic elastic modulus serves as an indicator of internal damage within NSRPC, where a higher value signifies greater integrity within the matrix and a lower degree of damage. Following the combined effects of fatigue and F-T cycles, the relative dynamic elastic modulus of NSRPC was depicted in Figure 13. As was anticipated, among all the mixtures, 0-PC exhibited the lowest relative dynamic elastic modulus following fatigue and F-T cycle effects with its dynamic elastic modulus of conditions being a mere 71.5% after enduring 2×10^5 fatigue cycles and 300 F-T cycles. The highest was found in 2-SF-PC at 86.2%. When the number of fatigue cycles was 0 and after 300 F-T cycles, the relative dynamic elastic modulus of 0-PC, 0.5-SF-PC, 1-SF-PC, 1.5-SF-PC, and 2-SF-PC had diminished by 19.5%, 14.9%, 11.8%, 6.5%, and 6.2%, respectively. When fatigue reached 2×10^5 cycles, following F-T cycles, the relative dynamic elastic modulus of 0-PC,

0.5-SF-PC, 1-SF-PC, 1.5-SF-PC, and 2-SF-PC had receded by 28.5%, 20.2%, 17.9%, 15.8%, and 13.6%, respectively. Comparable to mass loss rate, alterations to the relative dynamic elastic modulus were not drastic when the number of fatigue cycles was below 1×10^5. However, once fatigue surpassed 2×10^5 cycles, a significant plunge in the modulus of elasticity for NSRPC was observed.

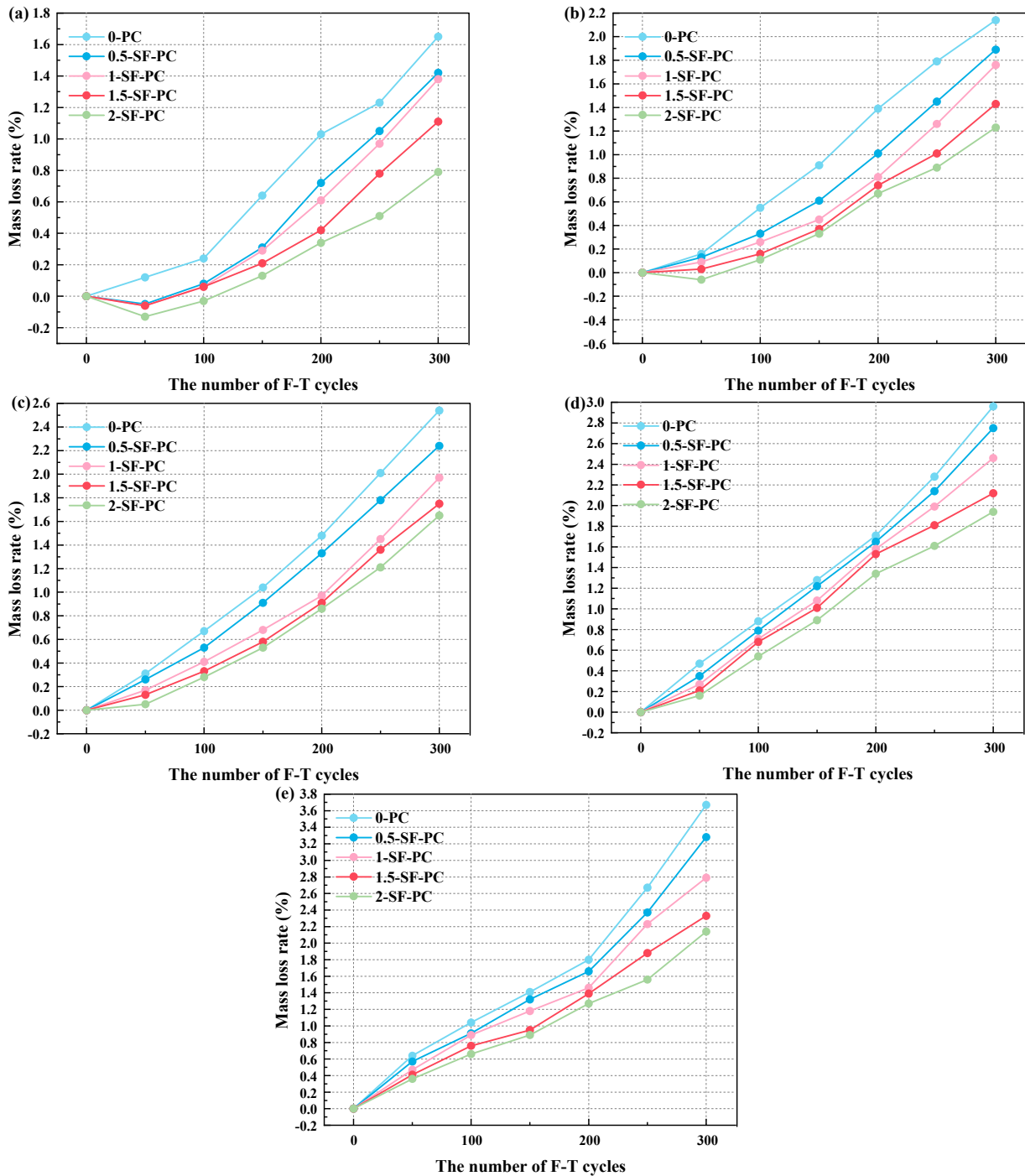**Figure 12.** Mass loss rate after different F-T and fatigue cycles: (**a**) N = 0, (**b**) N = 5.0 × 10⁴, (**c**) N = 1.0 × 10⁵, (**d**) N = 1.5 × 10⁵, (**e**) N = 2.0 × 10⁵.
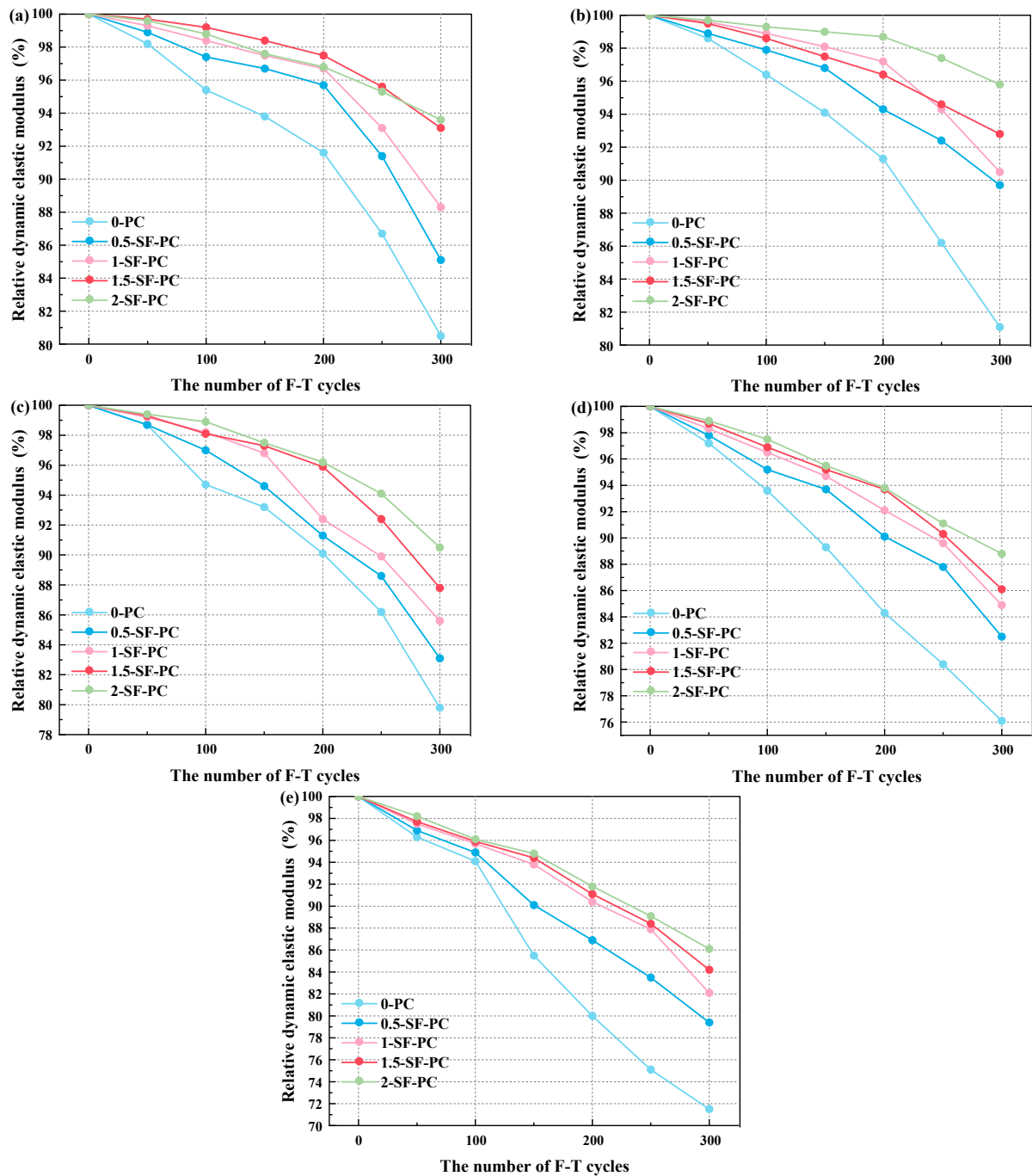
Figure 13. Relative dynamic elastic modulus after different F-T and fatigue cycles: (**a**) N = 0, (**b**) N = 5.0 × 10^4, (**c**) N = 1.0 × 10^5, (**d**) N = 1.5 × 10^5, (**e**) N = 2.0 × 10^5.

In comparison with 0-PC, with 0 fatigue cycles and 300 F-T cycles, the relative dynamic elastic modulus for 0.5-SF-PC, 1-SF-PC, 1.5-SF-PC, and 2-SF-PC witnessed growth of 4.6%, 7.7%, 13.0%, and 13.3%, respectively. Additionally, relative to 0-PC, with fatigue pegged at 2 × 10^5 cycles and 300 F-T cycles, the relative dynamic elastic modulus for 0.5-SF-PC, 1-SF-PC, 1.5-SF-PC, and 2-SF-PC inflated by 8.3%, 10.6%, 12.7%, and 14.9%, respectively. These data show that as the level of SF increased, the dynamic elastic modulus for NSRPC post F-T cycles consistently ascended. It also points out that the inclusion of SF better maintains the integrity and lessens the F-T damage of the NSRPC matrix. Coarse aggregates within traditional pervious concrete are simply bound by a thin layer of mortar, but passage

ways within NSRPC are filled with hardened concrete. Hence, compared to traditional pervious concrete, NSRPC exhibits superior fatigue and frost resistance.

3.4. Channel Characteristics

3.4.1. Deformation

Following the coupling of F-T and fatigue cycles, a permeability test was conducted. To analyze the changes in the permeability of NSRPC after fatigue and F-T cycles, the deformation of the NSRPC pores after F-T and fatigue cycles were examined. Figure 14 illustrates the relative deformation of the pore structure after different fatigue cycles. Throughout the different fatigue stages, there is no considerable discrepancy in the permeability of NSRPC, macroscopically demonstrating no evident destruction or deformation in the pore structure of NSRPC. The relative deformation predominantly occurs in the region subject to fatigue loading with relatively low deformation of the pore structure on either side of NSRPC. When the fatigue cycle is less than 5×10^4, the deformation of the pore structure in the area of stress concentration is between 3% and 6%, while the deformation on either side is merely between 1% and 3%, suggesting that the early phase fatigue load has a negligible impact on the NSRPC pore structure. However, when the fatigue cycle reaches 2×10^5, a substantial difference in the deformation of the NSRPC pore structure emerges. The deformation of the pore structure in the area of stress concentration increases to 12–26%, while the deformation on either side remains nearly unaltered, ranging from 3% to 7%. This could potentially indicate that the fatigue load principally affects the middle area of the NSRPC where the stress is concentrated [43].
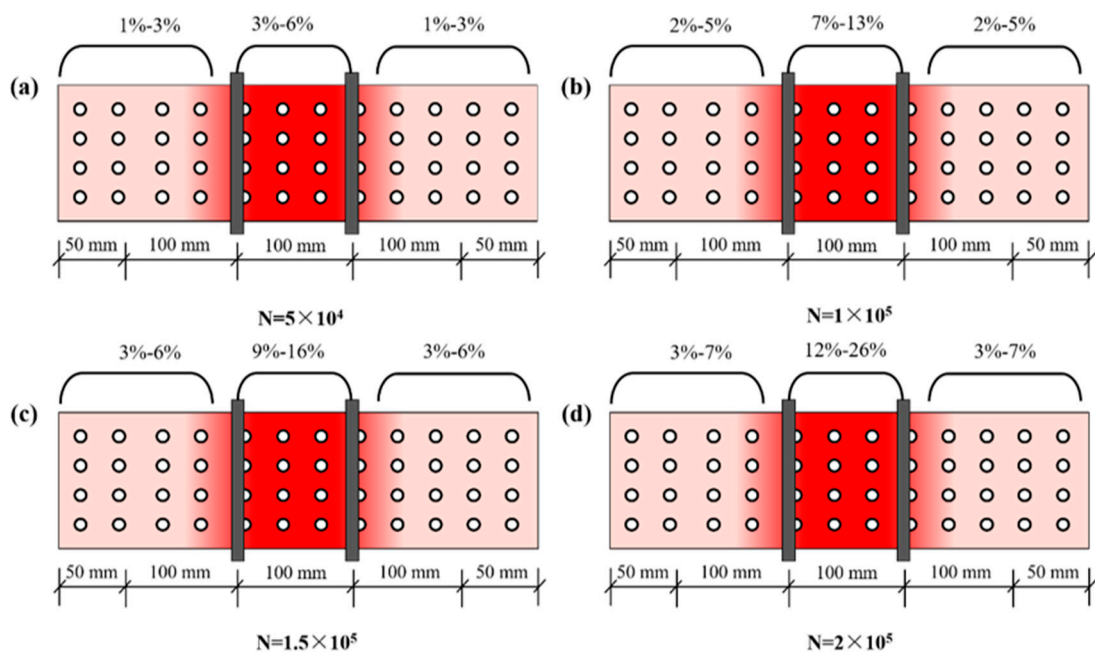

Figure 14. Pore channel deformation after fatigue cycles: (**a**) N = 5.0 × 10^4, (**b**) N = 1.0 × 10^5, (**c**) N = 1.5 × 10^5, and (**d**) N = 2.0 × 10^5.

3.4.2. Permeability Coefficient

Figure 15 serves to explicate the alterations in the permeability coefficient of NSRPC subject to the coupling of F-T and fatigue cycles. On the basis of the discrepancies in the number of fatigue instances, changes in the permeability coefficient may be segregated into two individual stages. In the primary phase, characterized by an absence of F-T cycles, the permeability coefficient of all NSRPCs remains virtually unaltered, indicating a marginal impact of the fatigue loads on the NSRPC permeability coefficient. During the secondary phase, occurring with a conjunction of fatigue and F-T cycles, the permeability coefficient manifests a notable initial decrease, which was followed by an increase as the number of

fatigue instances advances. At a fatigue cycle of 1×10^5, 0-PC, 0.5-SF-PC, 1-SF-PC, 1.5-SF-PC, and 2-SF-PC experience a decrease in their water permeability coefficients by 41.1%, 37.6%, 31.7%, 21.4%, and 27.9%, respectively, in comparison to NSRPC, which was devoid of any influence by the F-T effect. This indicates that even though a singular fatigue load has a lesser impact on the pore water permeability coefficient, the fatigue effect accelerates the formation of micro-cracks within the NSRPC matrix, thus rendering additional pathways for water intrusion. Consequently, a higher number of fatigue instances compromises the integrity of NSRPC matrix with the pore architecture facing significant F-T damage and consequent obstruction after F-T cycles. An increase in the permeability coefficient beyond a fatigue count of 1×10^5 does not denote a reduction in the F-T damages inflicted upon the NSRPC but rather indicates severe pore devastation, as the majority of the pore mortar detaches, accompanied by crack formation, indirectly enlarging the pore diameter and enhancing permeability of NSRPC.
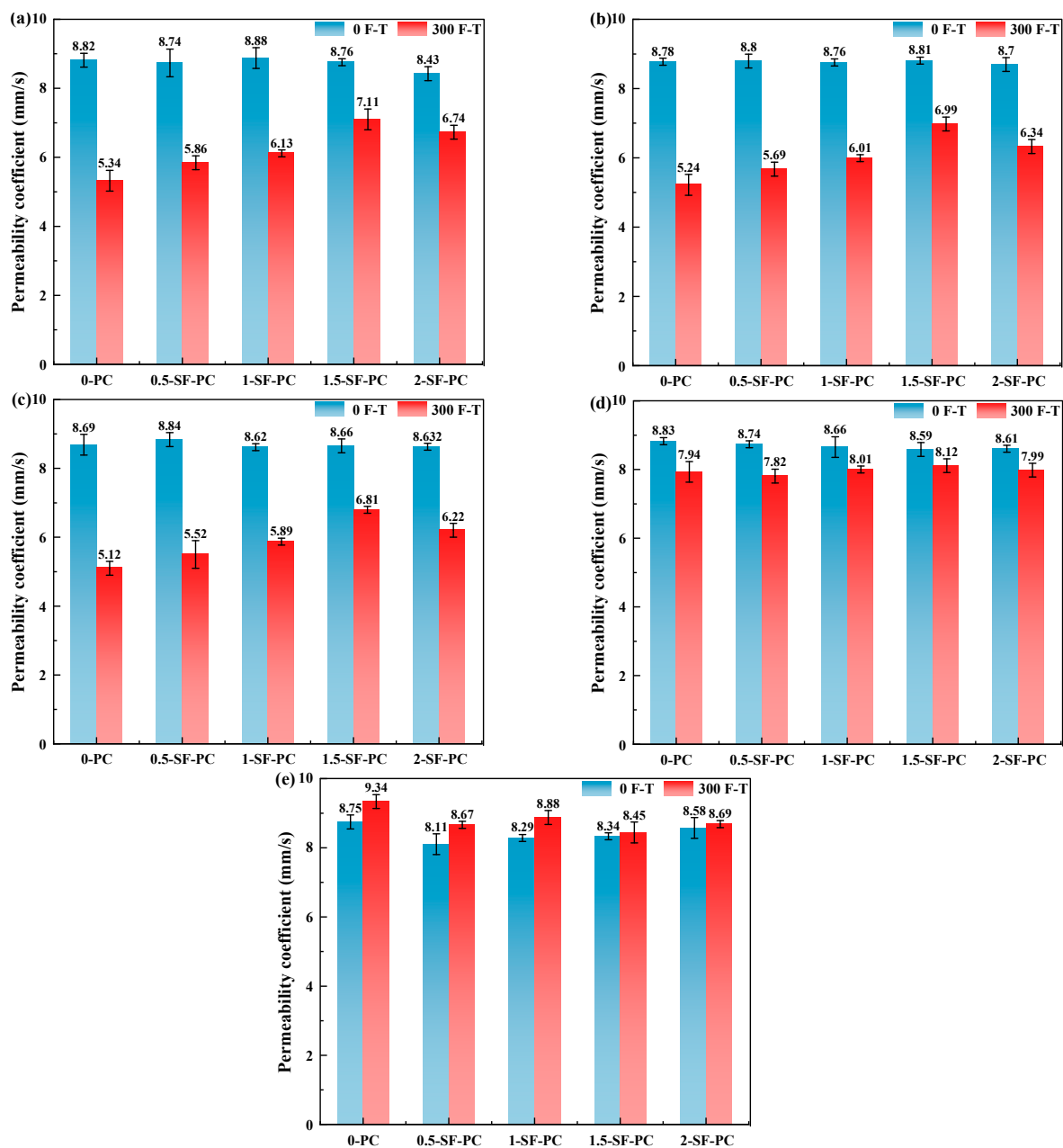

Figure 15. Change in permeability coefficient after coupling of F-T and fatigue cycles: (**a**) N = 0, (**b**) N = 5.0×10^4, (**c**) N = 1.0×10^5, (**d**) N = 1.5×10^5, and (**e**) N = 2.0×10^5.

In the ambit of all admixtures, after coupling of F-T and fatigue cycles, the lowest permeability coefficient is attributed to the control group, 0-PC, recorded merely at 5.1 mm/s, whereas 1.5-SF-PC manifests the optimum permeability, the coefficient being 6.8 mm/s. Even though the permeability coefficients of different admixtures evidenced no discernible pattern prior to F-T, all mixtures demonstrated varied degrees of decreased permeability at F-T cycle numbers, less than 1×10^5. In summation, the macroscopic permeability of NSRPC is marginally affected by fatigue load; however, on a microscopic level, the damages to the matrix by fatigue load exacerbate the loss of permeability coefficient in the subsequent stage. The integration of an appropriate volume of SF can temper the severity of the pore damage, thereby sustaining the permeability coefficient of NSRPC. Upon exceeding fatigue instances of 1×10^5, almost negligible differences are observed in the permeability coefficients of all mixtures before and after F-T cycles.

3.5. Rainstorm Waterlogging Resistance

3.5.1. Ponding Depth

As depicted in Figure 16, the ponding depth of NSRPC sets in the coupling of F-T and fatigue cycles. For mixtures without fatigue cycles, such as 1-SF-PC, 1.5-SF-PC, and 2-SF-PC, the ponding depth is below 40 mm. A tangible impact upon the ponding depth after the F-T cycles afflicts the surface of NSRPC. With an escalating number of fatigue cycles, the amassed water height inclines initially and then takes a downturn. An ascension of the ponding depth by 10.9% was observed after enduring 1×10^5 fatigue cycles, in comparison to the initial ponding depth without fatigue cycles. When the fatigue cycle count surpasses 1×10^5, the decline in ponding depth is principally due to two factors. Firstly, there is an accelerated accumulation speed brought about by intensified torrential rain, which, in accompaniment with the rising depth of the accumulated water, increases the water pressure atop the pores potentially rejuvenating F-T damaged pores. The other likelihood fields the shedding of mortar within the pore subsequent to the fatigue and F-T cycle, instigating the eruption of fractures between the pores, which indirectly augments the pore diameter. The highest ponding depth occurs with 0-PC following fatigue and F-T cycles, whereas 0.5-SF-PC, 1-SF-PC, 1.5-SF-PC and 2-SF-PC exhibit notable detriments to their surface water build-up as compared to 0-PC following torrential rain. The outcomes indicate that NSRPC incorporated with a suitable volume of SF show superior resistance to floodwater in torrential conditions following fatigue and F-T cycles. Furthermore, an inundated NSRPC surface does not necessarily imply internal flooding, as the permeability coefficient of NSRPC is more than 20 times the intensity of a centennial torrential downpour (4.5 mm/min) [44,45]. In simpler terms, the pores of NSRPC are perfectly capable of eliminating surplus rainfall. The formation of accumulated water typically results from localized pooling due to the uneven surface of the NSRPC. For 1.5-SF-PC and 2-SF-PC, the disparity in accumulated water depth, borne out of different periods, appears insignificant. These findings suggest that upon surpassing the 1.5% SF volume incorporation limit in NSRPC, the subsequent increase in SF exerts diminishing impacts on the pores of NSRPC, hence contributing only marginally to the alleviation of ponding depth.

3.5.2. Drainage Time

As illustrated in Figure 17, the drainage time of NSRPC altered under various combinations of fatigue and F-T cycles. After 1×10^5 fatigue cycles and 300 F-T cycles, the drainage time of 0.5-SF-PC, 1-SF-PC, 1.5-SF-PC, and 2-SF-PC were, respectively, 22.0%, 58.2%, 83.5%, and 89.0% lower than the reference group. Additionally, the drainage time of all specimens was considerably below the 15-minute stipulation of standard GB 51222-2017 [46], satisfying the requirements for flood prevention during the utilization period of secondary roads. The inclusion of SF effectively sustains the integrity of the pores, reduces blockages produced by F-T or fatigue cycles, and thus upholds permeability and diminishes drainage time. Remarkably, even without the incorporation of SF, 0-PC still meets the condition

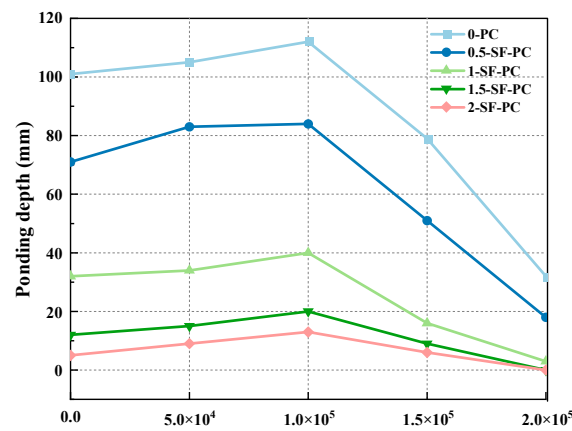that standing water dissipates within 15 min, satisfying the operational prerequisites of secondary roads.

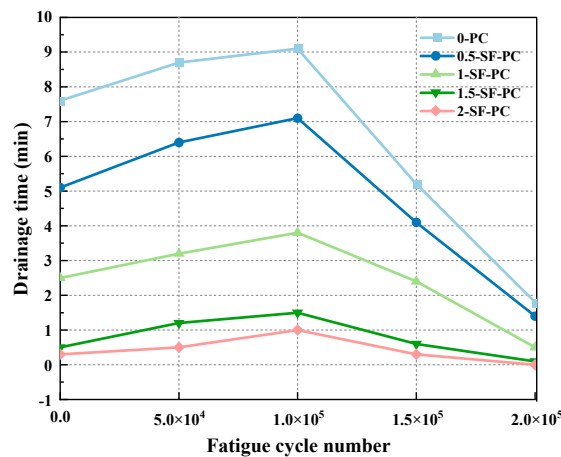**Figure 16.** Ponding depth of NSRPC after coupling of F-T and fatigue cycles.

Figure 17. Drainage time of NSRPC after coupling of F-T and fatigue cycles.

3.6. SEM Analysis

As demonstrated in Figure 18, the influence of fatigue and F-T cycle coupling on the SEM images of NSRPC became evident. Following the exertion from fatigue and F-T cycles, all admixtures displayed variable degrees of impairment. It was particularly noticeable in the vicinity of the interfacial transition zone where clear F-T destruction was discerned. An abundance of micropores and debris emerged adjacent to the mortar of the 0-PC aggregate with few through-cracks appearing on the surface. Furthermore, the surface of the 0.5-SF-PC also exhibited two perpendicular cracks, which was an indication that the fatigue load and F-T cycles inflicted noteworthy havoc on the microstructure within the NSRPC. Regarding the 1-SF-PC and 1.5-SF-PC, both exhibited far less damage than the 0-PC with SEM images revealing a relatively unscathed matrix devoid of conspicuous cracks or micropores. This signals that the introduction of an optimal volume of SF aided in preserving the integrity of the matrix. As for the 2-SF-PC, although its aggregate did not display noticeable F-T damage, the mortar between the aggregate showed signs of impairment, with the majority of it disintegrating into debris. This may potentially lead to partial macroscopic damage and even detachment in NSRPC.
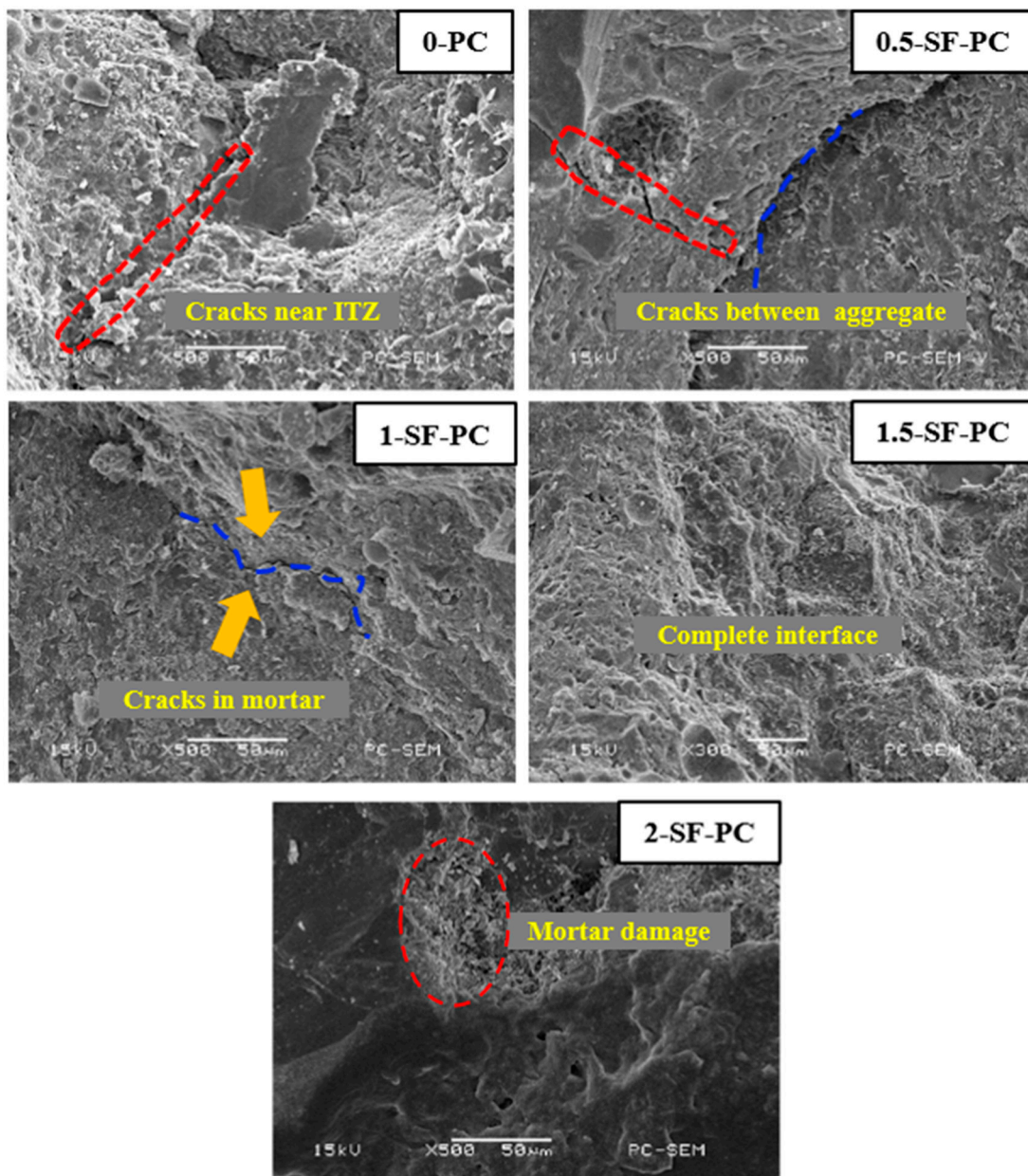
Figure 18. Microstructure of NSRPC after coupling of F-T and fatigue cycles.

4. Conclusions

1. The fatigue load exerts a detrimental impact on the compressive and flexural strength of NSRPC after F-T cycles with the role of SF in bolstering the flexural strength of NSRPC eclipsing their effect on its compressive strength. As the number of fatigue cycles increases, the compressive strength of NSRPC is decreasing. After 2×10^5 fatigue and 300 F-T cycles, NSRPC without SF experienced a fall in compressive and flexural strength by 49.9% and 51.5%, respectively, while the NSRPC including 1.5% SF suffered a reduction of just 26.4% and 29.7%.

2. In the early stage of fatigue cycle ($<1 \times 10^5$), the mass loss rate and relative dynamic elastic modulus of NSRPC changed little. With the increase in the number of fatigue cycles, the damage degree of NSRPC after F-T is deepened, the mass loss is gradually increased, and the relative dynamic elastic modulus is gradually reduced. After the coupling of fatigue and F-T cycles, the minimum mass loss rate of NSRPC is only 2.14%, and the relative dynamic elastic modulus can reach 86.2%.

3. With the increase in the number of fatigue cycles, the permeability coefficient of NSRPC after F-T cycles decreases first and then increases. The NSRPC with 1.5% and 2% SF maintains the integrity of the pores in the later stage of fatigue and F-T, so the permeability coefficient changes little.

4. Even with low SF content (<0.5 vol.%), the NSRPC after fatigue and F-T cycles still has excellent rainstorm resistance. Under the action of rainstorm in the 100-year return period, the maximum ponding depth is 84 mm, and the drainage time is 7.1 min, which meets the requirements of no rainstorm waterlogging during the rainstorm of the secondary highway.

5. In this study, the pore structure of NSRPC is relatively simple, and the mechanical properties, durability and rainstorm waterlogging resistance of NSRPC after fatigue or F-T cycles are quite different. Therefore, NSRPC with different porosity, pore diameter and pore arrangement should be analyzed in the future research so as to obtain the rainstorm waterlogging resistance of NSRPC with different porosity, pore diameter and pore arrangement after fatigue or F-T cycles. More importantly, the pore structure of NSRPC is an important internal factor affecting its service life. While considering the permeability, we should also pay attention to the influence of pore structure on the service life of NSRPC.

Author Contributions: Conceptualization, K.-L.H. and Y.S.; methodology, Y.S.; validation, K.-L.H., Y.S. and Y.-M.S.; formal analysis, K.-L.H.; investigation, Y.-M.S.; resources, K.-L.H.; data curation, Y.-M.S.; writing—original draft preparation, K.-L.H.; writing—review and editing, Y.S.; visualization, Y.-M.S.; supervision, Y.S.; project administration, Y.S.; funding acquisition, Y.S. All authors have read and agreed to the published version of the manuscript.

Data Availability Statement: The data that support the findings of this study are available from the corresponding author, [Yang Song], upon reasonable request.

Conflicts of Interest: The authors declare that they have no known competing financial interests or personal relationships that could have appeared to influence the work reported in this paper.

References

1. Cree, D.; Green, M.; Noumowé, A. Residual strength of concrete containing recycled materials after exposure to fire: A review. *Constr. Build. Mater.* **2013**, *45*, 208–223. [CrossRef]
2. Yang, J.; Jiang, G. Experimental study on properties of pervious concrete pavement materials. *Cem. Concr. Res.* **2003**, *33*, 381–386. [CrossRef]
3. Haselbach, L.M.; Valavala, S.; Montes, F. Permeability predictions for sand-clogged Portland cement pervious concrete pavement systems. *J. Environ. Manag.* **2006**, *81*, 42–49. [CrossRef] [PubMed]
4. Volder, A.; Watson, T.; Viswanathan, B. Potential use of pervious concrete for maintaining existing mature trees during and after urban development. *Urban For. Urban Green.* **2009**, *8*, 249–256. [CrossRef]
5. Xu, Q.; Jia, Z.; Tang, S.; Luo, W. The effect of flow partition on storm runoff and pollutant retention through raingardens with and without subsurface drainage. *J. Environ. Manag.* **2022**, *302*, 114038. [CrossRef] [PubMed]
6. AlShareedah, O.; Nassiri, S. Pervious concrete mixture optimization, physical, and mechanical properties and pavement design: A review. *J. Clean. Prod.* **2021**, *288*, 125095. [CrossRef]
7. Xie, Z.; Du, Q.; Cai, Z.; Liu, H.; Jamieson, S. Courtyard-level sewer data-enhanced two-dimensional hydraulic model for urban flood hazard assessment in Kunming, China. *Water Policy* **2015**, *17*, 143–161. [CrossRef]
8. Zhang, X.; Hu, M.; Chen, G.; Xu, Y. Urban Rainwater Utilization and its Role in Mitigating Urban Waterlogging Problems-A Case Study in Nanjing, China. *Water Resour. Manag.* **2012**, *26*, 3757–3766. [CrossRef]
9. Du, S.; Rompaey, A.V.; Shi, P.; Wang, J.a. A dual effect of urban expansion on flood risk in the Pearl River Delta (China) revealed by land-use scenarios and direct runoff simulation. *Nat. Hazards* **2015**, *77*, 111–128. [CrossRef]
10. Lund, M.S.M.; Hansen, K.K.; Brincker, R.; Jensen, A.H.; Amador, S.D.R. Evaluation of freeze-thaw durability of pervious concrete by use of operational modal analysis. *Cem. Concr. Res.* **2018**, *106*, 57–64. [CrossRef]

11. Dreelin, E.A.; Fowler, L.; Ronald Carroll, C. A test of porous pavement effectiveness on clay soils during natural storm events. *Water Res.* **2006**, *40*, 799–805. [CrossRef] [PubMed]

12. Adresi, M.; Yamani, A.; Karimaei Tabarestani, M.; Rooholamini, H. A comprehensive review on pervious concrete. *Constr. Build. Mater.* **2023**, *407*, 133308. [CrossRef]

13. Wu, F.; Yu, Q.; Brouwers, H.J.H. Mechanical, absorptive and freeze–thaw properties of pervious concrete applying a bimodal aggregate packing model. *Constr. Build. Mater.* **2022**, *333*, 127445. [CrossRef]

14. Lima, G.T.d.S.; Rocha, J.C.; Cheriaf, M. Investigation of the properties of pervious concrete with a recycled aggregate designed with a new combination of admixture. *Constr. Build. Mater.* **2022**, *340*, 127710. [CrossRef]

15. Pradhan, S.K.; Behera, N. Performance assessment of pervious concrete road on strength and permeability by using silica fume. *Mater. Today Proc.* **2022**, *60*, 559–568. [CrossRef]

16. Li, J.; Zhang, Y.; Liu, G.; Peng, X. Preparation and performance evaluation of an innovative pervious concrete pavement. *Constr. Build. Mater.* **2017**, *138*, 479–485. [CrossRef]

17. Kia, A.; Wong, H.S.; Cheeseman, C.R. High-strength clogging resistant permeable pavement. *Int. J. Pavement Eng.* **2021**, *22*, 271–282. [CrossRef]

18. Richardson, A.E.; Coventry, K.A.; Wilkinson, S. Freeze/thaw durability of concrete with synthetic fibre additions. *Cold Reg. Sci. Technol.* **2012**, *83–84*, 49–56. [CrossRef]

19. Xianglong, L.; Ze, Z.; Andrey, M.; Mingyi, Z.; Doudou, J.; Jinbang, Z. Variation of Ground Surface Freezing/Thawing Index in China under the CMIP6 Warming Scenarios. *Sustainability* **2022**, *14*, 14458.

20. Taheri, B.M.; Ramezanianpour, A.M.; Sabokpa, S.; Gapele, M. Experimental evaluation of freeze-thaw durability of pervious concrete. *J. Build. Eng.* **2021**, *33*, 101617. [CrossRef]

21. Luo, G.; Zhao, P.; Zhang, Y.; Xie, Z. Performance Evaluation of Waste Crumb Rubber/Silica Fume Composite Modified Pervious Concrete in Seasonal Frozen Regions. *Adv. Mater. Sci. Eng.* **2021**, *2021*, 1411185. [CrossRef]

22. Tarangini, D.; Sravana, P.; Srinivasa Rao, P. Effect of nano silica on frost resistance of pervious concrete. *Mater. Today Proc.* **2022**, *51*, 2185–2189. [CrossRef]

23. Pan, J.; Shen, Y.; Yang, G.; Zhang, H.; Yang, H.; Zhou, Z. Debonding behaviors and micro-mechanism of the interface transition zone in sandstone-concrete interface in response to freeze-thaw conditions. *Cold Reg. Sci. Technol.* **2021**, *191*, 103359. [CrossRef]

24. Zhang, J.; Meng, B.; Wang, Z.; Xiong, J.; Tang, W.; Tan, Y.; Zhang, Z. Numerical simulation on cleaning of clogged pervious concrete pavement. *J. Clean. Prod.* **2022**, *341*, 130878. [CrossRef]

25. Sandoval, G.F.B.; Jussiani, E.I.; de Moura, A.C.; Andrello, A.C.; Toralles, B.M. Hydraulic and morphological characterization of clogged pervious concrete (PC). *Constr. Build. Mater.* **2022**, *322*, 126464. [CrossRef]

26. Zou, D.; Wang, Z.; Shen, M.; Liu, T.; Zhou, A. Improvement in freeze-thaw durability of recycled aggregate permeable concrete with silane modification. *Constr. Build. Mater.* **2020**, *268*, 121097. [CrossRef]

27. Singh, A.; Sampath, P.V.; Biligiri, K.P. A review of sustainable pervious concrete systems: Emphasis on clogging, material characterization, and environmental aspects. *Constr. Build. Mater.* **2020**, *261*, 120491. [CrossRef]

28. Chandrappa, A.K.; Biligiri, K.P. Pervious concrete as a sustainable pavement material—Research findings and future prospects: A state-of-the-art review. *Constr. Build. Mater.* **2016**, *111*, 262–274. [CrossRef]

29. Jiao, K.; Chen, C.; Li, L.; Shi, X.; Wang, Y. Compression Fatigue Properties of Pervious Concrete. *ACI Mater. J.* **2020**, *117*, 241.

30. Chandrappa, A.K.; Biligiri, K.P. Flexural-fatigue characteristics of pervious concrete: Statistical distributions and model development. *Constr. Build. Mater.* **2017**, *153*, 1–15. [CrossRef]

31. AlShareedah, O.; Nassiri, S.; Dolan, J.D. Pervious concrete under flexural fatigue loading: Performance evaluation and model development. *Constr. Build. Mater.* **2019**, *207*, 17–27. [CrossRef]

32. *GB/T 25177-2010*; Recycled Coarse Aggregate for Concrete. China Architecture and Building Press: Beijing, China, 2010.

33. *GB/T 50081-2019*; Standard for Test Methods of Concrete Physical and Mechanical Properties. China Architecture and Building Press: Beijing, China, 2019.

34. *GB/T 50082-2009*; Standard for Test Methods of Long-Term Performance and Durability of Ordinary Concrete. China Architecture and Building Press: Beijing, China, 2009.

35. Zhu, P.; Shi, Z.; Liu, H.; Yan, X.; Yang, L.; Zong, M. Pore Characteristic Design Method of High-strength Pervious Concrete Based on the Mechanical Properties and Rainstorm Waterlogging Resistance. *J. Wuhan Univ. Technol.-Mater. Sci. Ed.* **2023**, *38*, 567–574. [CrossRef]

36. Bai, J.; Xu, R.; Zhao, Y.; Shi, J. Flexural fatigue behavior and damage evolution analysis of aeolian sand concrete under freeze–thaw cycle. *Int. J. Fatigue* **2023**, *171*, 107583. [CrossRef]

37. Xue, G.; Zhu, H.; Xu, S.; Dong, W. Fatigue performance and fatigue equation of crumb rubber concrete under freeze–thaw cycles. *Int. J. Fatigue* **2023**, *168*, 107456. [CrossRef]

38. Liu, D.; Wang, C.; Gonzalez-Libreros, J.; Guo, T.; Cao, J.; Tu, Y.; Elfgren, L.; Sas, G. A review of concrete properties under the combined effect of fatigue and corrosion from a material perspective. *Constr. Build. Mater.* **2023**, *369*, 130489. [CrossRef]

39. Li, Z.; Shang, H.; Xiao, S.; Yang, L.; Li, Z. Effect of thermal fatigue on mechanical properties and microstructure of concrete in constant ambient humidity. *Constr. Build. Mater.* **2023**, *368*, 130367. [CrossRef]

40. Wang, D.; Zhao, Q.; Yang, C.; Chi, Y.; Qi, W.; Teng, Z. Study on frost resistance and vegetation performance of seashell waste pervious concrete in cold area. *Constr. Build. Mater.* **2020**, *265*, 120758. [CrossRef]

41. Toghroli, A.; Mehrabi, P.; Shariati, M.; Trung, N.T.; Jahandari, S.; Rasekh, H. Evaluating the use of recycled concrete aggregate and pozzolanic additives in fiber-reinforced pervious concrete with industrial and recycled fibers. *Constr. Build. Mater.* **2020**, *252*, 118997. [CrossRef]

42. Grabias-Blicharz, E.; Franus, W. A critical review on mechanochemical processing of fly ash and fly ash-derived materials. *Sci. Total Environ.* **2023**, *860*, 160529. [CrossRef]

43. Cui, K.; Xu, L.; Li, L.; Chi, Y. Mechanical performance of steel-polypropylene hybrid fiber reinforced concrete subject to uniaxial constant-amplitude cyclic compression: Fatigue behavior and unified fatigue equation. *Compos. Struct.* **2023**, *311*, 116795. [CrossRef]

44. Hou, J.; Mao, H.; Li, J.; Sun, S. Spatial simulation of the ecological processes of stormwater for sponge cities. *J. Environ. Manag.* **2019**, *232*, 574–583. [CrossRef] [PubMed]

45. Qian, J.; Du, Y.; Yi, J.; Liang, F.; Huang, S.; Wang, X.; Wang, N.; Tu, W.; Pei, T.; Ma, T. Regional geographical and climatic environments affect urban rainstorm perception sensitivity across China. *Sustain. Cities Soc.* **2022**, *87*, 104213. [CrossRef]

46. *GB 51222-2017*; Technical Code for Urban Flooding Prevention And Control. China Architecture and Building Press: Beijing, China, 2017.